Nanoscale

PAPER

Strongly exchange coupled inverse ferrimagnetic soft/hard, Mn$_x$Fe$_{3−x}$O$_4$/Fe$_x$Mn$_{3−x}$O$_4$, core/shell heterostructured nanoparticles†

A. López-Ortega,[a] M. Estrader,*[ab] G. Salazar-Alvarez,[b] S. Estradé,[cd] I. V. Golosovsky,[e] R. K. Dumas,[f] D. J. Keavney,[g] M. Vasilakaki,[h] K. N. Trohidou,[h] J. Sort,[ij] F. Peiró,[c] S. Suriñach,[j] M. D. Baró[j] and J. Nogués[ai]

Inverted soft/hard, in contrast to conventional hard/soft, bi-magnetic core/shell nanoparticles of Mn$_x$Fe$_{3−x}$O$_4$/Fe$_x$Mn$_{3−x}$O$_4$ with two different core sizes (7.5 and 11.5 nm) and fixed shell thickness (∼0.6 nm) have been synthesized. The structural characterization suggests that the particles have an interface with a graded composition. The magnetic characterization confirms the inverted soft/hard structure and evidences a strong exchange coupling between the core and the shell. Moreover, larger soft core sizes exhibit smaller coercivities and loop shifts, but larger blocking temperatures, as expected from spring-magnet or graded anisotropy structures. The results indicate that, similar to thin film systems, the magnetic properties of soft/hard core/shell nanoparticles can be fine tuned to match specific applications.

1. Introduction

Core/shell (CS) nanoparticles are an efficient way to construct multicomponent systems that combine the distinct properties of the diverse constituents in a single structure.[1] Importantly, the advantage of multicomponent nanostructures lies not only in their multifunctionality, but also in the possibility to improve and tune the single-phase properties using the interactions between the different components. Moreover, the recent advances in wet chemistry synthesis have allowed an unprecedented control of the structural parameters (*e.g.*, size, shape and composition) of the particles which leads to the possibility to fine tune the different functionalities of these multiphase systems.[2–4] In the search for materials suitable for permanent magnets, biomedical applications, sensing applications, and future magnetic recording media, bi-magnetic CS nanoparticles, where both core and shell are magnetic materials, are attracting a great deal of interest, particularly since an inherent exchange bias can be used to overcome the superparamagnetic limit.[5] In this context, standard and "inverse" bi-magnetic CS systems involving antiferromagnetic (AFM) and ferromagnetic (FM) phases structured as FM/AFM or AFM/FM have been extensively studied in the recent years.[6–14] Interestingly, the so-called "exchange-spring" magnets,[15] where hard and soft magnetic phases are exchange coupled, have been the focus of renewed effort in thin film systems for recording applications,[16] although less attention has been paid to the case of nanoparticles.[17] These bi-component materials can exhibit the desirable properties of both phases, *i.e.* large coercivities and large magnetization arising from the hard and soft phases, respectively.[15] Hard–soft nanocomposites such as FePt–Fe$_3$Pt,[18] NdFeB–FeCo,[19,20] NdFeB–Fe,[21,22] FePt–Fe$_3$O$_4$ (ref. 23 and 24) and FePt–CoFe$_2$O$_4$ (ref. 25) heterodimers have been prepared by mechanical milling,[19–21] self-assembly processes[18] or wet-chemistry.[22–25] However, the limited intimate contact between both phases in heterodimer systems and the reduced homogeneity in the case of nanocomposites and self-assembly processes make these materials non-ideally suited to accomplish strong exchange coupling and enhanced properties. In this regard, core/shell nanoparticles, where the interface contact is maximized, would be more adequate. Hard/soft core/shell nanoparticles composed

[a]CIN2(ICN-CSIC) and Universitat Autònoma de Barcelona, Catalan Institute of Nanotechnology, Campus de la UAB, 08193 Bellaterra (Barcelona), Spain. E-mail: martaestrader@gmail.com

[b]Department of Materials and Environmental Chemistry, Stockholm University, 10691 Stockholm, Sweden

[c]LENS-MIND-IN2UB, Departament d'Electrònica, Universitat de Barcelona, Martí i Franquès 1, E-08028 Barcelona, Spain

[d]TEM-MAT, SCT, Universitat de Barcelona, Barcelona, Spain

[e]St Petersburg Nuclear Physics Institute, Gatchina, 188300 St Petersburg, Russia

[f]Department of Physics, University of Gothenburg, 41296 Gothenburg, Sweden

[g]Advanced Photon Source, Argonne National Laboratory, Argonne, Illinois 60439, USA

[h]Institute of Materials Science, NCSR "Demokritos", 153 10 Aghia Paraskevi, Attiki, Greece

[i]Institució Catalana de Recerca i Estudis Avançats (ICREA), Barcelona, Spain

[j]Departament de Física, Universitat Autònoma de Barcelona, 08193 Bellaterra, Spain

† Electronic supplementary information (ESI) available: Simulated elemental quantification at a given core/shell structure, XAS and XMCD spectra of CS2 nanoparticles and hysteresis loops after FC and ZFC for both CS1 and CS2 samples. See DOI: 10.1039/c2nr30986f

of FePt/Fe$_3$O$_4$,[24,26–30] Fe/Fe$_3$O$_4$,[31,32] CoFe$_2$O$_4$/MFe$_2$O$_4$ (M = Zn, Mn, Fe)[33] and Sm(Co$_{1−x}$Fe$_x$)/Fe$_3$O$_4$ (ref. 34) have shown, in some cases, an enhanced energy product of the bi-component system over the hard single phase.[25,32,35] On the other hand, "inverse" soft/hard core/shell configurations have been less studied, and only a few examples, FePt/CoFe$_2$O$_4$,[30] MFe$_2$O$_4$/CoFe$_2$O$_4$ (M = Zn, Mn, Fe)[33] and γ-Fe$_2$O$_3$/CoFe$_2$O$_4$,[36] have been reported. There are a number of issues that are well known from thin film studies on spring-magnets that have not been addressed in nanoparticles. Amongst these are the strong dependence of the properties on the thickness of the two constituents[37] and the enhancement of the properties by inter-mixed interfaces[35] or graded anisotropy (i.e., where the anisotropy changes *continuously* from hard to soft).[38]

Herein we present an exhaustive structural and magnetic study of inverted soft/hard core/shell nanoparticles composed of Mn$_x$Fe$_{3−x}$O$_4$/Fe$_x$Mn$_{3−x}$O$_4$ with two different core sizes (7.5 and 11.5 nm) and a fixed shell thickness (∼0.6 nm) obtained by seeded growth of manganese oxide using different Fe$_3$O$_4$ nanoparticles as seeds. The smooth hysteresis loops obtained from magnetometry and the compelling similarity between the element resolved loops obtained by soft X-ray magnetic circular dichroism indicate a strong core/shell exchange coupling. Furthermore, we show that the magnetic properties, e.g., saturation magnetization, coercivity, loop shift or blocking temperature, are easily controlled by adjusting the size of the soft core.

2. Experimental

2.1. Synthesis

Unless stated, all starting materials were purchased from Sigma-Aldrich and used without further purification. The CS nanoparticles were synthesized following an earlier reported procedure where, in two steps, pre-made Fe$_3$O$_4$ nanoparticles were used as seeds to subsequently grow a Mn$_3$O$_4$ layer.[39] Firstly, Fe$_3$O$_4$ seeds were prepared following a similar method to that developed by Park et al.[40] in which a given amount of iron (III) oleate and 1 mmol of oleic acid were added into 36 mL of 1-octadecene. The mixture was heated under magnetic stirring, with a heating rate of 3 °C min$^{−1}$, up to 320 °C and kept for 30 min. The slurry was removed from the heating source and allowed to cool down to room temperature. Depending on the surfactant-to-metal molar ratio, [S]/[M], different particle sizes were obtained. Two [S]/[M] ratios were studied: [S]/[M] = 0.6 (*seed1* – large particles) and [S]/[M] = 0.3 (*seed2* – small particles).

Subsequently, the heterogeneous growth of the manganese oxide layer was carried out at the surface of the two different seeds following a slightly modified literature process by adding 42 mg of initial seeds in a solution containing 0.6 mmol of manganese (II) acetylacetonate, 0.6 mmol of 1,2-hexadecanediol, 0.3 mmol of oleylamine, 0.3 mmol of oleic acid and 40 mL of dibenzyl ether.[39] The slurry was mechanically stirred and heated, under an Ar controlled atmosphere, with a heating rate of 10 °C min$^{−1}$, to 200 °C and kept for 1 h. The flask was removed from the heating source and cooled down in Ar to 180 °C. The solution was then exposed to air and allowed to cool to room temperature. Two different CS particles were obtained based on two seeds, i.e. CS1 (from the large seed1) and CS2 (from the small seed2). Both the Fe$_3$O$_4$ seeds and the CS nanoparticles were washed by several cycles of coagulation with ethanol, centrifugation at 2000 × g, disposal of supernatant solution and re-dispersion in hexane.

2.2. Characterization

Transmission electron microscopy. TEM images were obtained using a Jeol JEM-2010 microscope with a LaB$_6$ filament and a Jeol-JEM-2010F microscope with a field-emission gun operated at 200 kV. The nanoparticles were dispersed in hexane and then placed dropwise onto a holey carbon supported grid. The particle size of the different samples and its standard deviation were obtained by calculating the average number by manually measuring the equivalent diameters of >200 particles from TEM micrographs.

X-ray diffraction. XRD patterns were collected using a Panalytical X'Pert Pro diffractometer with Cu Kα radiation. The measurements were carried out in a range of 10–100 2θ in steps of 0.012° and collection time of 300 s. All diffraction patterns were analyzed using the FullProf code.[41] Note that a simple fitting of the diffraction patterns by the Rietveld method using an isotropic approximation gives rise to unsatisfactory results due to non-uniform size effects. In these cases the numerical computation of the scattering intensity on the Debye formula was used.[42] The diffraction profiles were satisfactorily described by implementing an artificial shape (platelet-like) for the shell component. Finally note that the diffraction signal from the shell is exceedingly weak to reliably refine the sizes and stoichiometry.

Electron energy loss spectroscopy. EEL spectra were acquired every 0.5 nm along the diameter of the nanoparticles at an energy range containing the O K, Mn L$_{2,3}$ and Fe L$_{2,3}$ edges, with an energy resolution of 0.8 eV. Mn/O and Fe/O quantifications were carried out using the Gatan Digital Micrograph commercial software. Importantly, data obtained for different particles of the CS1 sample showed no relevant differences.

X-ray absorption spectroscopy and X-ray magnetic circular dichroism. XAS and XMCD measurements were performed on dried CS nanoparticles spread onto carbon tape at the 4-ID-C beamline of the Advance Photon Source of the Argonne National Laboratory. Both XAS and XMCD spectra were recorded at the Fe and Mn L$_{2,3}$ edges using total electron yield (TEY) mode at 10 K in a magnetic field of 50 kOe after field cooling (FC) from 300 K under an applied field of 50 kOe. The element resolved XMCD hysteresis loops, for the Fe and Mn L$_3$ edges, were acquired by recording the field dependence of the XMCD signals at the energies corresponding to the three main peaks of the Fe-edge (i.e., 707.6, 708.7, 709.3 eV) and for the main energy of the Mn edge (640.1 eV). The XMCD signal was normalized by the area of the XAS spectra after correcting for the background. Note that since the Fe edge loops at the different energies were analogous only the one at E = 709.3 eV is used in the discussion.

Magnetic measurements. The magnetic properties of the nanoparticles were measured on tightly packed powdered samples using a superconducting quantum interference device (SQUID, Quantum Design) magnetometer with a 70 kOe maximum field. The magnetization *versus* temperature measurements were performed in zero field cooled (ZFC) and field cooled (FC) conditions in 50 Oe. After FC in 20 kOe from 300 K to 10 K, hysteresis loops were measured at different constant temperatures. Moreover, hysteresis loops were also measured at 10 K after ZFC from 300 K.

In addition to standard major loop measurements, a first-order reversal curve (FORC)[43–46] analysis was conducted using the following procedure. After positive saturation the applied field is reduced to a given reversal field, H_R. From this reversal field the magnetization is then measured back towards positive saturation, thereby tracing out a single FORC. This process is repeated for a series of decreasing reversal fields, thus filling the interior of the major hysteresis loop, which can be seen as the outer boundary of the family of FORCs. The FORC distribution is then defined as a mixed second order derivative of the normalized magnetization:

$$\rho(H, H_R) \equiv -\frac{1}{2}\frac{\partial^2 M(H, H_R)/M_S}{\partial H \partial H_R}, \tag{1}$$

which is then plotted against (H, H_R) coordinates on a contour map. For a given reversal field, H_R, the magnetization is measured for increasing applied fields, H, and therefore $H \geq H_R$ by design. Following the measurement procedure the FORC distribution is read in a "top-down" fashion and from left to right for a particular reversal field. The FORC distribution provides a useful "fingerprint" of the reversal mechanism by mapping out, in (H, H_R) coordinates, only the *irreversible* switching processes. It is often useful to have a one-dimensional visualization of the irreversibility by projecting the FORC distribution onto the H_R-axis. This is equivalent to an integration over the applied field H:

$$\int \frac{\partial^2 M(H, H_R)}{\partial H \partial H_R}\, dH = \frac{\partial M(H_R)}{\partial H_R}, \tag{2}$$

and is termed a FORC-switching field distribution (FORC-SFD).

Monte Carlo simulations. Monte Carlo simulations were carried out considering a single spherical nanoparticle of radius R, expressed in lattice spacings, on a simple cubic lattice, with FiM order. The nanoparticle consists of a soft core (either 10.7 or 16.7 lattice spacings) and a hard shell of thickness equal to 3 lattice spacings. The outer layer of one lattice spacing is considered to be the surface of the nanoparticle. We use atomic-scale modeling where the spins in the particle interact with nearest neighbors Heisenberg exchange interaction, and at each crystal site they experience a uniaxial anisotropy. We consider the size of the atomic spins in the two sublattices of the FiM particle equal to 1 and 3/2, respectively, for both the core and the shell. The energy of the system includes the exchange interaction between the spins in the nanoparticle and the single-site anisotropy energy terms. In the presence of an external magnetic field, the total energy of the system is:

$$\mathcal{H} = -J_{core}\sum_{i,j \in core} \vec{S}_i \cdot \vec{S}_j - J_{IF}\sum_{i \in core, j \in shell} \vec{S}_i \cdot \vec{S}_j - J_{shell}\sum_{i,j \in shell} \vec{S}_i \cdot \vec{S}_j$$

$$-K_{core}\sum_{i \in core}(\vec{S}_i \cdot \hat{e}_i)^2 - K_{IF}\sum_{i \in IF}(\vec{S}_i \cdot \hat{e}_i)^2 - K_{shell}\sum_{i \in shell}(\vec{S}_i \cdot \hat{e}_i)^2$$

$$-K_{srf}\sum_{i \in srf}(\vec{S}_i \cdot \hat{e}_i)^2 - \vec{H} \cdot \sum_i \vec{S}_i. \tag{3}$$

Here S_i and $\hat{e}_i$ are the atomic spin and the unit vector in the direction of the easy axis at site i. The first three terms give the Heisenberg nearest neighbor exchange interaction between the spins in the core, in the shell and at the interface. We set exchange coupling as $J_{core} = -0.01J$ in the core, where J is defined as a dimensionless ferromagnetic exchange coupling constant taken as $J = 1$, $J_{IF} = 4 \times J_{core}$ at the interface and smaller in the shell ($J_{shell} = 0.5 \times J_{core}$) to account for its lower transition temperature. The following four terms are the anisotropy energies of the core, the interface, the shell and the surface, respectively. The anisotropy is assumed uniaxial and directed along the z-axis in the core, the shell and at the interface and random at the surface. The last term is the Zeeman energy. The anisotropies in the conventional core/shell structure are taken as $K_{core} = 0.01J$, $K_{IF} = 0.03J$, $K_{shell} = 0.08J$ and $K_{surf} = 0.6J$, respectively.

Importantly, to account for the chemical gradients, we also considered the case of graded anisotropy, similar to thin film systems.[38,47] For such structures, the anisotropy energy term of the core or the shell is split into different layers. For example, we have considered that the inner core K_{core} is maintained constant at $0.01J$, while as the layers get closer to the interface the anisotropy gradually increases as 0.02, 0.03, 0.04, 0.05 and 0.06J (for the top 5 layers in the core) and 0.07 and 0.08J for the shell and finally we maintain $K_{surf} = 0.6J$.

To take into consideration the random distribution of easy axis directions with respect to the applied fields present experimentally, we have calculated hysteresis loops for different angles between the easy axis and the applied field direction. The results for the magnetization are averaged as:

$$\langle M \rangle = \frac{1}{4\pi}\int_0^{2\pi} d\varphi \int_0^\pi d\theta M(\theta)\cos\theta = \frac{1}{2}\int_0^\pi d\theta M(\theta)\cos\theta \tag{4}$$

Note that the different parameters are given with respect to J, *i.e.*, the field H is given in units of $J\,g^{-1}\,\mu_B^{-1}$, the temperature T in units $J\,k_B^{-1}$ and the anisotropy coupling constants K in units of J. The magnetization M is normalized to the saturation magnetization, M_S.

The Monte Carlo simulations are performed using the Metropolis algorithm[48] where the microstructure and the temperature are explicitly included. We perform our calculations of the hysteresis loops at a low temperature after a field cooling procedure at a constant rate for a cooling field of $H_{FC} = 0.4\,J\,g^{-1}\,\mu_B^{-1}$, which is in the same field range as the one used experimentally.

3. Results and discussion

3.1. Structural and morphological characterization

Fig. 1 shows the transmission electron microscopy (TEM) images of the Fe_3O_4 seeds (Fig. 1a and b for samples seed1 and seed2,

respectively) and the CS nanoparticles (Fig. 1c and d for samples CS1 and CS2, respectively). Particle size histograms of both the seeds and the CS nanoparticles are depicted in Fig. 1e and f corresponding to samples seed1–CS1 and seed2–CS2, respectively. As can be seen, all histograms are well fitted by a Gaussian distribution, showing a unique size population, with a narrowly distributed diameter (deviation <10%). After the growth of the Mn oxide layer, the diameter of the CS nanoparticles becomes 8.6(0.6) (CS2) and 12.6(1.0) (CS1) compared to the initial 7.5(0.6) nm (seed2) and 11.5(0.9) nm (seed1), respectively. Importantly, upon comparing the sizes of the seeds and CS nanoparticles, there is a clear shift of 1.1 nm to larger diameters both for CS1 and CS2 samples, indicating that a Mn oxide shell of roughly 0.6 nm thickness is indeed grown on top of the seeds. Moreover, the similarity between the thicknesses of the two shells suggests that the seed-growth procedure does not depend strongly on the initial seed size.

High resolution TEM (HR-TEM) images of seed2, CS1 and CS2 and their respective fast Fourier transform (FFT) are shown in Fig. 2. The FFT analysis obtained from the HR-TEM images of the CS samples (Fig. 2e and f) confirms the presence of a new phase in contrast to the data of the seeds which display a purely cubic structure (Fig. 2d). In both CS samples two sets of different

diffraction spots attributed to an iron oxide cubic spinel phase [$(111)_c$ $d = 0.481$ nm, $(220)_c$ $d = 0.290$ nm, $(311)_c$ $d = 0.248$ nm and $(331)_c$ $d = 0.180$ nm (JCPDS card no. 82-1533)] and a manganese oxide tetragonal spinel phase [$(200)_t$ $d = 0.288$ nm, $(211)_t$ $d = 0.248$ nm, $(004)_t$ $d = 0.237$ nm and $(204)_t$ $d = 0.183$ nm (JCPDS card no. 24-0734)] can be observed. Remarkably, while the tetragonal $(200)_t$, $(211)_t$ and $(204)_t$ diffraction planes overlap with the cubic $(220)_c$, $(311)_c$ and $(331)_c$ ones, the plane $(004)_t$ (highlighted by arrows in Fig. 2e and f) belongs only to a tetragonal spinel phase.

The analysis of the XRD patterns corresponding to the iron oxide seeds and the CS nanoparticles (Fig. 3) revealed that the sizes of the seeds are similar to the corresponding core sizes of the CS nanoparticles (see Table 1). Moreover, these values are consistent with those obtained from TEM analysis. Interestingly, the refinement of the site occupancies shows that both the core and the seeds have a near stoichiometric spinel Fe_3O_4 composition. However, there are small differences in the occupancy of the seeds, i.e., $(Fe_{0.82(1)})[Fe_{0.90(1)}]_2O_4$ and the CS particles, i.e., $(M_{0.90(1)})[M_{0.96(1)}]_2O_4$ (M = Fe and Mn) which imply that probably some Mn ions have diffused into the core during the synthesis of the CS particles. Note that it is not possible to distinguish between iron and manganese ions using X-rays, hence it is difficult to give a more quantitative account of the manganese diffusion. A comparison of the refined cell parameters for the core with the reported values for the Mn_3O_4–Fe_3O_4 system[49] indicates that the core can incorporate up to 50% of Mn atoms. Concerning the shell, the comparison of the obtained cell parameters with the literature values[49] unambiguously evidences that in sample CS1 about 10% of manganese ions of the Mn_3O_4 shell are substituted by iron ions, while maintaining the Mn_3O_4 tetragonal structure.

In order to gain further insight into the structure of the CS particles, the local electron energy loss spectra (EELS) were analyzed by evaluating the M–$L_{2,3}$ onset and the M/O ratio (M = Mn and Fe) to obtain the distributions of the different ions across the particles, see Fig. 4. The EELS analysis reveals the presence of two clearly differentiated regions in the particle, i.e., a core and a shell, the former being iron rich and the latter one manganese rich. However, remarkably, both iron and manganese ions were found across the whole particle (Fig. 4e). Bearing in mind these results, together with the XRD and FFT studies where the existence of a tetragonal spinel phase was confirmed, different CS structures (i.e., sizes and compositions) were simulated to match the observed metal distribution. The best correspondence was found for a $MnFe_2O_4$(10.2 nm)/$FeMn_2O_4$(1.2 nm) CS structure, as schematically shown in Fig. 4b, with an iron rich core and a manganese rich shell. Interestingly, using compositional gradients throughout the particles (rather than fixed core/shell structures) e.g., $Mn_{0.75}Fe_{2.25}O_4$(8 nm)/$Fe_{1.75}Mn_{1.25}O_4$(0.6 nm) shell 1/$Fe_{1.5}Mn_{1.5}O_4$(0.6 nm) shell 2/$Fe_{0.75}Mn_{2.25}O_4$(0.6 nm) shell 3, leads to a further improvement of the agreement between the simulated and experimental results (see Fig. S1 in the ESI†). It is known that mixed spinel phases can preserve their initial crystal symmetry before reaching a critical doping value, for instance $MnFe_2O_4$ ($Fd3m$) and $FeMn_2O_4$ ($I41/amd$) would keep the cubic and tetragonal structure of Fe_3O_4 and Mn_3O_4, respectively.[49] The results indicate that an interdiffusion of iron and manganese
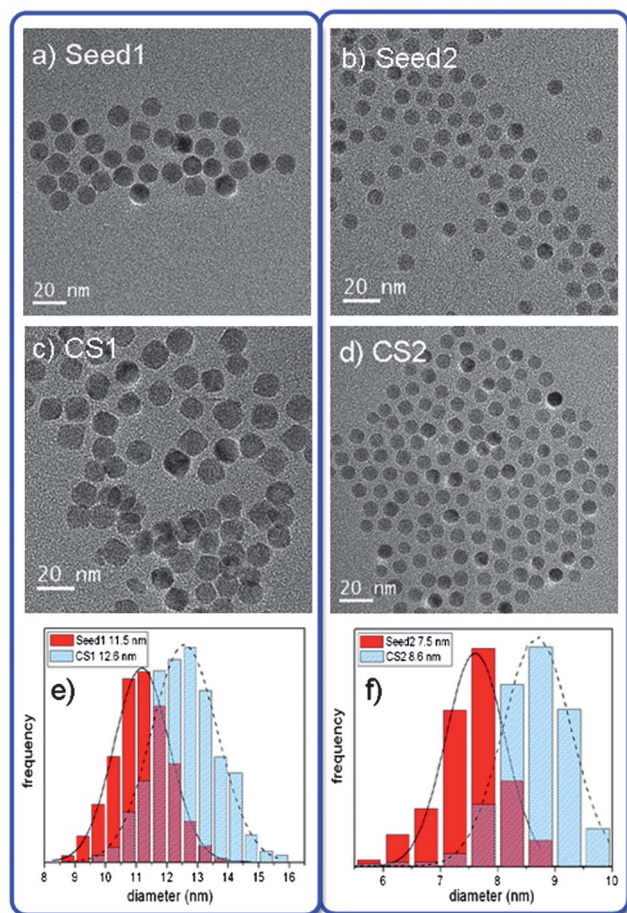
Fig. 1 TEM images of iron oxide seed particles, (a) seed1 and (b) seed2 and of the corresponding CS nanoparticles, (c) CS1 and (d) CS2. Histograms of the different nanoparticles, (e) seed1–CS1 and (f) seed2–CS2.
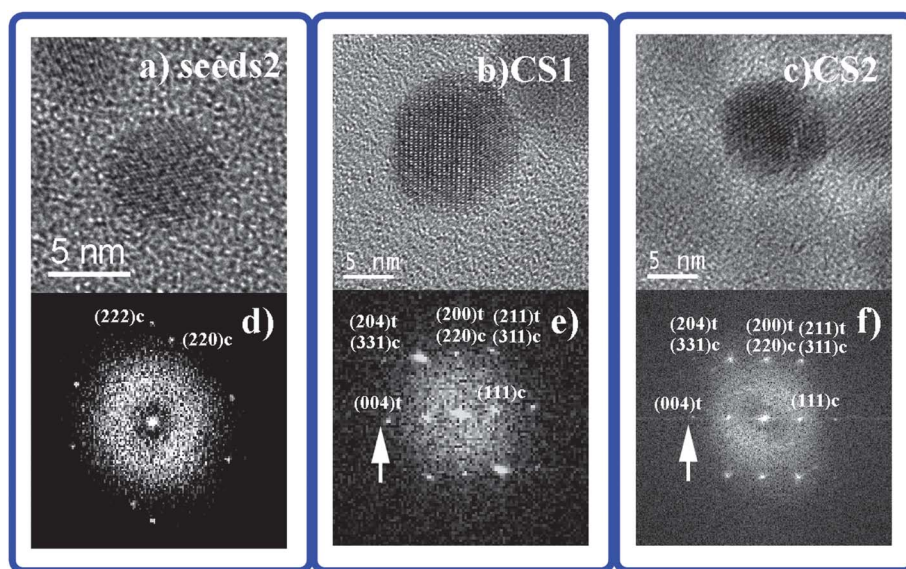
Fig. 2 HR-TEM images of (a) seed2, (b) CS1 and (c) CS2 nanoparticles together with their respective FFT analysis, (d–f). The diffraction spots in FFT images for cubic and tetragonal structures are marked with c and t, respectively. The pure tetragonal spots are highlighted by arrows.
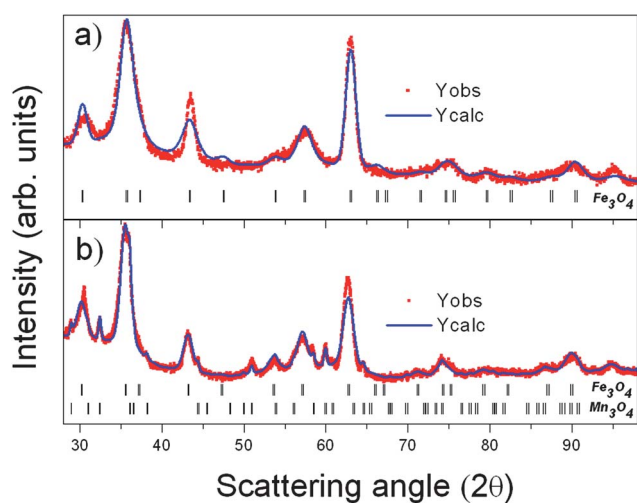
Fig. 3 Profile analysis of the X-ray diffraction patterns from seed1 (a) and the CS1 nanoparticles (b). The observed profile (in red) and the calculated (in blue) are both shown in the graphs. The vertical bars mark the position of Bragg reflections as indicated.

Table 1 Unit cell parameters and sizes (both in Å) for the different seeds and CS nanoparticles. The figure in parenthesis corresponds to the standard deviation in the last digit

Core Fe_3O_4			Shell Mn_3O_4	
Sample	a	Size	a	c
CS1	8.3801(6)	93(1)	5.767(1)	9.414(2)
Seed1	8.3501(5)	91(2)		
CS2	8.3803(5)	73(1)	5.775(1)	9.432(2)
Seed2	8.343(1)	68(3)		

ions between core and shell has taken place leading to mixed Fe–Mn spinel CS particles.[50] The ion diffusion and the concomitant change in the composition of the CS nanoparticles

can be attributed to a soft annealing while exposing the slurry to air at 180 °C. Note that the nanoparticles in sample CS2 displayed a rather poor signal-to-noise ratio since, given the small size of CS2 nanoparticles, the signal at the Fe- and Mn-edges was rather weak compared to the carbon signal arising from the organic surfactants and thus the EEL Spectra for CS2 were not analysed.

Additional evidence for the graded composition of the CS particles was obtained by using X-ray absorption spectroscopy (XAS) and X-ray magnetic circular dichroism (XMCD). Importantly, the total electron yield (TEY) mode depends on the probing depth (λ_x), which for soft X-rays can be taken to be of the order of 10 nm for most metal oxides.[51] Assuming such λ_x and that the nanoparticles are composed of, approximately, 85%-$MnFe_2O_4$/15%-$FeMn_2O_4$, the spectra should be understood as a convolution of the signal from the shell and the core. Fig. 5 shows an example of XAS and XMCD spectra obtained at Fe and Mn $L_{2,3}$ edges for sample CS1. From the theoretical XAS spectra of Fe^{2+} ions in octahedral and Fe^{3+} ions in octahedral and tetrahedral environments, the peak I_1 in Fig. 5b can be associated to the presence of Fe^{2+} in Oh positions while peak I_2 correlates to Fe^{3+} ions located in Oh and Td environments.[52] By analyzing the ratio of the different peak intensities, I_1/I_2, it is possible to obtain qualitative information about the cation concentration in each oxide phase.[53] Given the structure of Fe_3O_4, $(Fe^{3+})[Fe^{3+}Fe^{2+}]O_4$, and γ-Fe_2O_3, $(Fe^{3+})[Fe^{3+}_{5/3} \square_{1/3}]O_3$ one would expect I_1/I_2 ratios of 0.53 and 0.19 for Fe_3O_4 and γ-Fe_2O_3, respectively.[51] The experimental I_1/I_2 value for both samples CS1 and CS2 is 0.4. This implies that the samples have an intermediate composition between γ-Fe_2O_3 and Fe_3O_4. Therefore, the presence of a $MnFe_2O_4$ structure, $(Fe^{3+})[Fe^{3+}Mn^{2+}]O_4$,[52,54] without Fe^{2+} ions in octahedral positions, would fit adequately in this scenario in agreement with the EELS results (particularly assuming that due to the thin shell with small iron content most of the XAS iron signal arises from the core). On the other hand the XAS spectrum at the Mn $L_{2,3}$ edge (Fig. 5a) resembles that of pure tetragonal
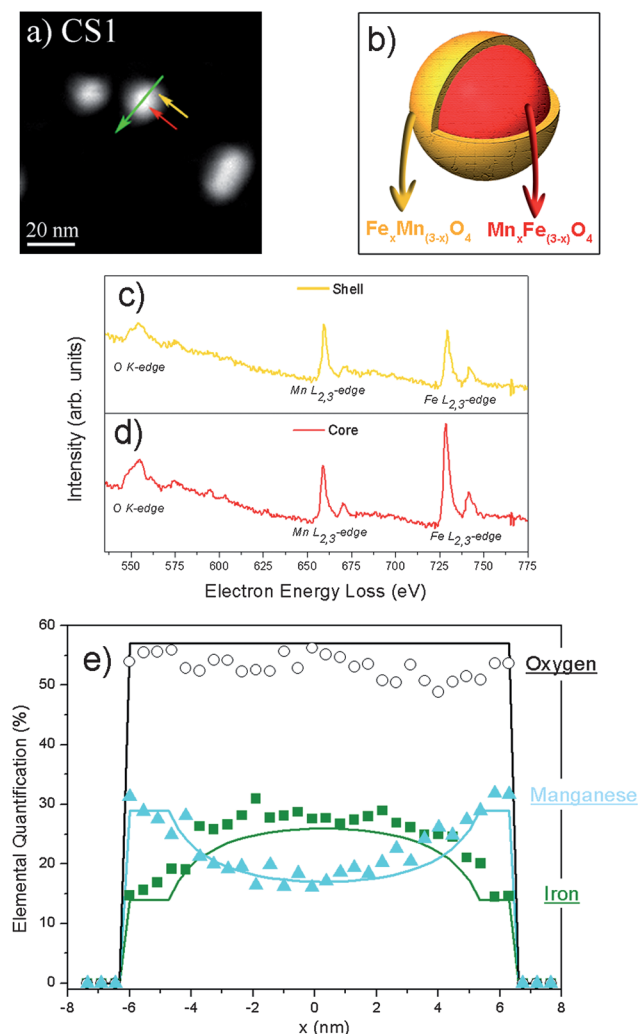
Fig. 4 (a) High-angle annular dark field (HAADF) image of CS1 nanoparticles, where the approximate positions where the local spectra were obtained are shown by a green arrow. (b) Schematic representation of the CS nanoparticles simulated from the EELS analysis. (c) and (d) show EELS spectra for the shell and core, respectively, as indicated by yellow and red arrows, respectively, in (a). (e) Elemental quantification along the particle diameter for Fe (squares), Mn (triangles) and O (circles). The solid lines represent the simulated elemental profile for a particle with a $MnFe_2O_4$(10.2 nm) core/$FeMn_2O_4$(1.2 nm) shell structure.

Mn_3O_4, $(Mn^{2+})[Mn^{3+}]_2O_4$.[55] However, it has a lower intensity ratio, $I'_1/I'_2 = 0.7$, than expected for Mn_3O_4, i.e., $I'_1/I'_2 = 0.87$, but larger than the corresponding one for $MnFe_2O_4$, $I'_1/I'_2 = 0.5$.[54] Hence, the Mn $L_{2,3}$ signal can be understood as a mixed signal arising both from the shell, close to a tetragonal $FeMn_2O_4$ phase, and the core, with a cubic $MnFe_2O_4$ structure.

Concerning the XMCD spectra, the signal of the iron edge (Fig. 5d) is somewhat consistent with those of pure cubic spinel iron oxides (Fe_3O_4 and γ-Fe_2O_3) spectra,[53] although some small deviations attributed to the presence of the mixed $MnFe_2O_4$ oxide can be observed. Concretely, the different intensity peak ratios of the first two peaks of the iron XMCD signal with respect to pure iron oxides can be interpreted in the same way as the XAS analysis regarding the concentration of Fe^{2+} ions in octahedral positions.[54,56] In contrast, the spectrum at the manganese
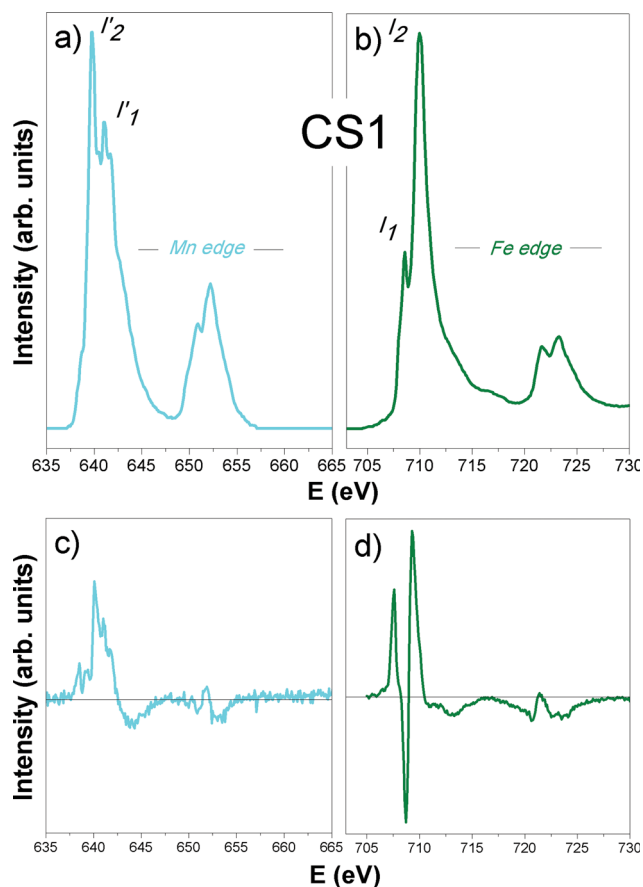

Fig. 5 (Top) XAS and (bottom) XMCD spectra at the (left) Mn and (right) Fe edges of CS1 nanoparticles.

edge (Fig. 5c) cannot be associated to any single phase and can be clearly ascribed to a mixed XMCD signal, e.g., arising from tetragonal $FeMn_2O_4$ and cubic $MnFe_2O_4$ oxide structures.[55] Note that the lack of XMCD studies at the Mn $L_{2,3}$ edge on pure $FeMn_2O_4$ (in bulk or nanoparticle form) makes a more detailed analysis rather complex. Similar results were found for CS2 nanoparticles, both for the XAS and XMCD analysis, see Fig. S2†.
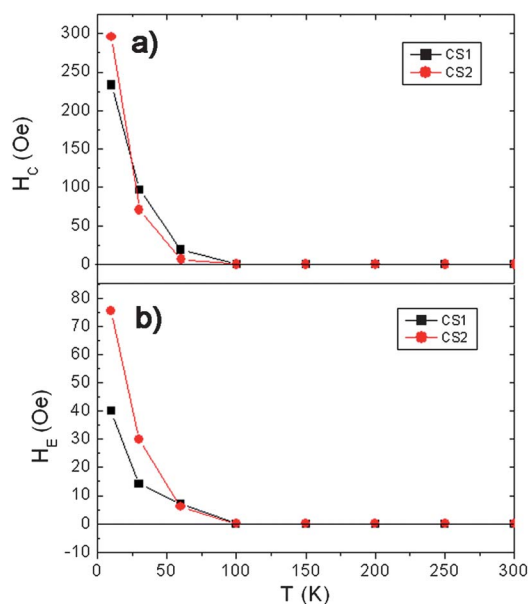
3.2. Magnetic properties

Fig. 6a shows the ZFC/FC magnetization curves for the CS1 and CS2 nanoparticles. Although at high temperatures both samples exhibit the characteristics of superparamagnetic systems[57] with blocking temperatures, $T_{B,1}^{CS1} = 205$ K and $T_{B,1}^{CS2} = 115$ K, both systems exhibit a second transition at $T_{B,2} \sim 40$ K. However, the features at $T_{B,2}$ are more evident for CS2. Moreover, as can be seen in Fig. 6b, the low temperature (10 K) hysteresis loops show that the saturation magnetization, M_S, for CS1 ($M_S^{CS1} = 48$ emu g^{-1}) is higher than that for CS2 ($M_S^{CS2} = 40$ emu g^{-1}). Upon enlarging it becomes clear that the loops are rather smooth, i.e., no kinks – typical of two phase systems –[15] can be observed, Fig. 6b. Interestingly, both samples exhibit a loop shift in the field axis, H_E (i.e., exchange bias), with respect to the zero field cooled loop (Fig. S3†), and moderate coercivities, H_C,[6] that vanish around 50–60 K, both parameters being larger for CS2 (Fig. 7).
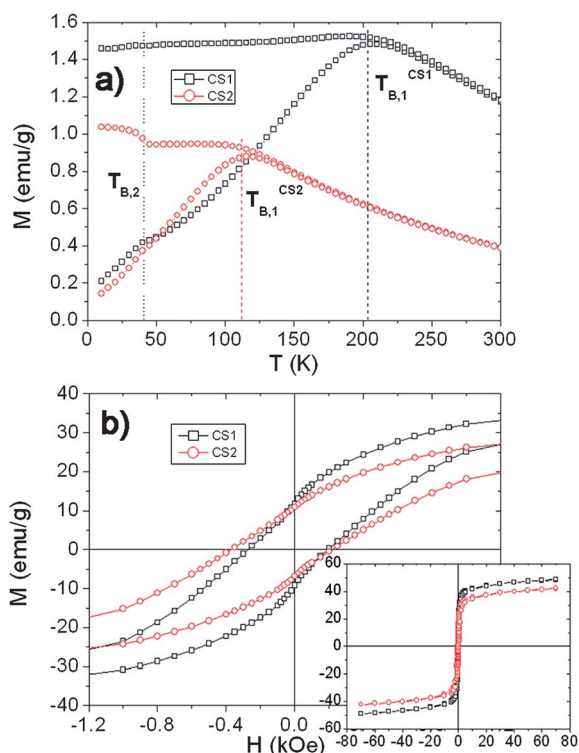
Fig. 6 (a) Temperature dependence of the field cooled (FC) and zero field cooled (ZFC) magnetizations and (b) an enlarged view at low field of the hysteresis loops at 10 K for CS1 and CS2 nanoparticles. The inset shows the hysteresis loops in the full field range.

Fig. 7 Temperature dependence of (a) the coercivity, H_C, and (b) the loop shift, H_E, for CS1 and CS2 nanoparticles. The lines are guides to the eye.
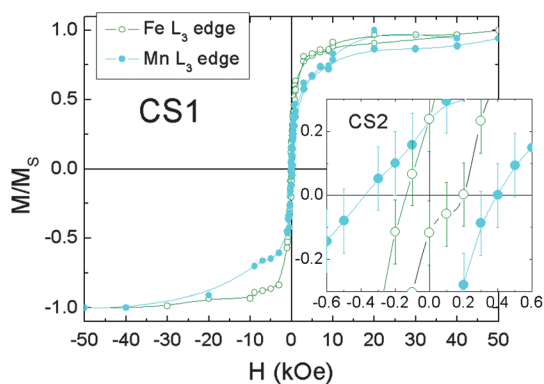
These results are consistent with the proposed $Mn_xFe_{3-x}O_4/Fe_xMn_{3-x}O_4$ core/shell structure. Concerning the different T_B, the high temperature ones ($T_{B,1}$) could be related to the cubic ferrimagnetic (FiM) $Mn_xFe_{3-x}O_4$ phase that constitutes the core of the nanoparticle, while the low temperature one ($T_{B,2}$) to the tetragonal FiM $Fe_xMn_{3-x}O_4$ phase forming the shell. Thus, the lower $T_{B,1}$ for CS2 can be easily explained by its smaller core volume since $T_B = KV/25\ k_B$,[57] (where K is the magnetic anisotropy, V the volume and k_B the Boltzmann constant). In fact, assuming that the anisotropies remain the same in both cores, the ratio $T_{B,1}^{CS2}/T_{B,1}^{CS1}$ leads to a volume ratio in rough concordance with the initial seed sizes. In principle, similar effects should occur for $T_{B,2}$ since, although the shell thickness is the same for both systems, the core sizes vary and the corresponding shell volumes should be different. The origin of this $T_{B,2}$ is probably two-fold. First, $FeMn_2O_4$ is known to have a very strong temperature dependence of K, with a sharp increase in K around 50–60 K.[58,59] Thus, when K reaches a certain threshold the system becomes blocked. Moreover, since the $Fe_xMn_{3-x}O_4$ shell phase exhibits a tetragonal structure with a non-stoichiometric structure, probably close to that of Mn_3O_4 (as hinted from the XRD lattice parameters and the EELS graded composition simulation), a magnetic behaviour similar to that of Mn_3O_4 could be expected. In this sense, the second temperature transition present in both samples, $T_{B,2} \sim 40$ K, would be consistent with the $T_C = 40$ K of bulk Mn_3O_4, as expected from the strong dependence of T_C on the Mn content for Mn-rich $Fe_xMn_{3-x}O_4$.[49,60,61] Similarly, the larger M_S

exhibited by CS1 is consistent with its larger core, since the relative contribution of the shell (with a smaller M_S than that of the core[62]) should be smaller for larger particles. This core/shell volume ratio also explains the more prominent features at $T_{B,2}$ shown by CS2.

Concerning the presence of exchange bias and moderate coercivities, although these effects are expected for an exchange coupled antiferromagnetic AFM/FM systems, they can also be found in coupled soft FiM (or FM) and hard FiM (or FM).[6] In the current core/shell nanoparticles, assuming the composition of the shell is in the range Mn_3O_4–$FeMn_2O_4$, at 10 K the anisotropy would be expected to be about $|K_{shell}| \sim 5 \times 10^5$ to 1×10^6 erg cm^{-3}.[58,63,64] In contrast, if the core composition is in the range Fe_3O_4–$MnFe_2O_4$, the corresponding anisotropy would be $|K_{core}| \sim 2 \times 10^5$ erg cm^{-3}.[58,65] Consequently, our core/shell particles can be considered as an 'inverted' soft/hard system, although the difference in $K_{shell} - K_{core}$ may not be as large as in some of the typical hard/soft spring-magnet systems.[15]
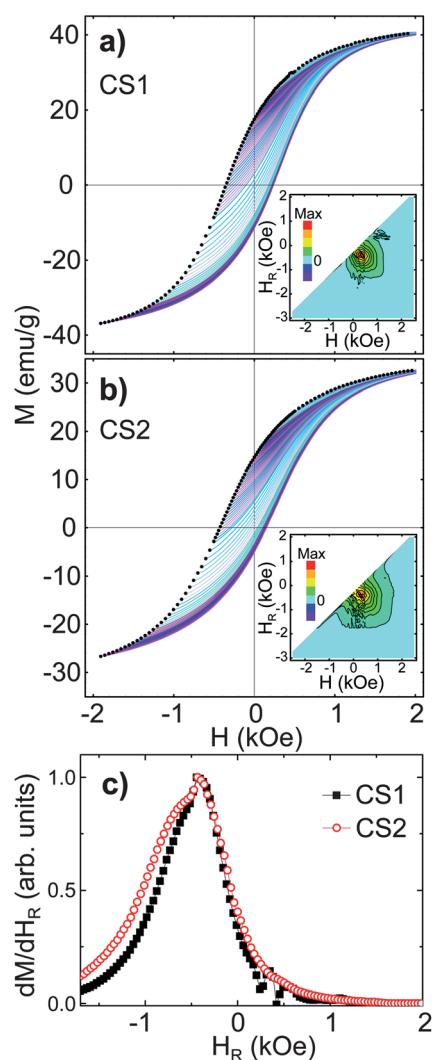
In AFM/FM thin film systems it is well established that H_C and H_E are inversely proportional to the thickness (size) of the FM phase. Thereby, by drawing an analogy, in soft/hard systems it is accepted that H_C, $H_E \propto 1/size_{(soft-FM)}$. Thus, the smaller H_E and H_C for CS1 arise from the larger diameter of its core. Finally, the temperature dependence of H_C and H_E is controlled by the phase with lowest T_B, $i.e.$, the hard shell phase, in analogy with most of the standard AFM/FM systems.[6] Interestingly, the coercivity of both CS particles is relatively small compared with that expected for Mn_3O_4–$FeMn_2O_4$ (forming the shell).[12] In analogy with thin film systems, this implies that the soft core and the hard shell are strongly exchange coupled as expected from their small size (smaller than the domain wall width) and their similar anisotropies.[15,37] This leads to smooth loops with increased M_S and reduced H_C, with respect to the pure hard Mn_3O_4 phase.

To gain further insight into the core/shell structure of the nanoparticles, we acquired element-specific XMCD hysteresis loops at the iron and manganese edges (shown in Fig. 8). Although the overall shape of the XMCD hysteresis loops at both edges is rather similar, their approach to saturation shows clear differences. Namely, the loop taken at the iron edge saturates at considerably lower fields than the loop corresponding to manganese (see Fig. 8 for CS1). Remarkably, H_C of both elements is similar for both samples. However, while for CS1 $H_C(\text{Mn})$ and $H_C(\text{Fe})$ are roughly the same, within the error, for CS2 $H_C(\text{Mn})$ is slightly larger than $H_C(\text{Fe})$ (see inset in Fig. 8). These results are in concordance with the magnetometry hysteresis loops where CS2, with proportionally more Mn, exhibits both an enhanced H_C and larger saturation field than those of CS1. The element resolved loops allow us to assign these features to the presence of a magnetically harder manganese-based phase. Given that, nominally, the iron and the manganese hysteresis loops should mainly correspond to the core and the shell, respectively, the element specific hysteresis loops confirm the inverse soft/hard core/shell structure of the nanoparticles. Importantly, the similarities between the Fe and Mn contributions to the hysteresis loops imply again a strong coupling between the core and the shell. However, the concomitant overlap of diverse contributions in the XMCD spectra (due to simultaneous interdiffusion of iron and manganese ions between the core and the shell) makes a quantitative analysis rather complex.

The coupling between the core and shell is further investigated by analyzing the first order reversal curves (FORC). The measured family of FORC curves is shown in Fig. 9a and b for samples CS1 and CS2, respectively. The major loop, seen as the outer boundary of the FORCs, shows the expected exchange bias. The resultant FORC distributions, shown as insets in Fig. 9a and b, are both broad single peaks, consistent with prior nanoparticle FORC distributions.[44] The broadness of the peaks can be attributed to distributions in size, anisotropy easy axis direction and strength, and exchange coupling. The FORC switching field distributions (FORC-SFDs), plotted in Fig. 9c, show a clear asymmetry for both the CS1 and CS2 samples, where the initial rapid onset of reversal ($H_R \sim +500$ Oe) is

Fig. 9 Families of FORCs, whose starting points are represented by black dots, for samples (a) CS1 and (b) CS2 with the corresponding FORC distributions plotted in (H, H_R) coordinates shown as insets. The resultant FORC-SFDs are shown in (c).

followed by a more gradual and extended switching tail towards negative H_R values. Similar asymmetric FORC-SFDs have been observed in hard/soft and graded anisotropy composite films[38b,45,46] where the extended hump can be attributed to the more negative H_R needed to switch the high anisotropy components. Note that single phase nanoparticles similar to the core (i.e., without shell) exhibit symmetric peaks in the FORC-SFD. Interestingly, sample CS2 approaches negative saturation more gradually than CS1, suggesting a more dominant hard phase component, which is also consistent with the larger exchange bias and coercivity observed in this sample at 10 K.

The hysteresis loops were simulated by using Monte Carlo based on a (a) conventional core/shell model (i.e., a single value for the interface anisotropy; Fig. 10a) (b) a graded anisotropy model (Fig. 10b). As can be seen in the figures, both approaches capture the main features of the experimental loops. For example, the smaller nanoparticles exhibit larger H_C and H_E than the bigger ones. Similarly, in the moderate field range the small particles have a broader loop both in the experimental and

Fig. 8 Element resolved XMCD hysteresis loop at the iron edge (709.3 eV – open symbols) and manganese edge (640.1 eV – filled symbols) for sample CS1. The inset shows an enlargement of the hysteresis loops for sample CS2. The lines are guides to the eye.
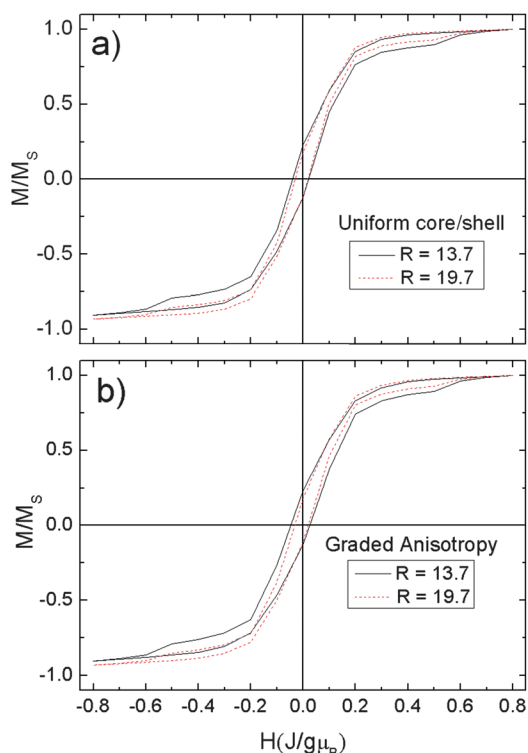
Fig. 10 Simulated hysteresis loops for the $R = 13.7$ and 19.7 lattice spacings nanoparticles using a (a) uniform core/shell and (b) graded anisotropy models of the nanoparticles.

simulated loops. Moreover, the calculations clearly show that the high field features are dominated by the shell, as hinted by the XMCD results. Most importantly, the ratio of core/shell anisotropies needed to properly simulate the experimental loops is in concordance with the core/shell anisotropy ratio of the phases deduced from the structural characterization. Hence, the Monte Carlo simulations confirm the strongly exchange coupled inverse soft/hard core/shell structure of the nanoparticles. Finally, comparing the simulation of the conventional core/shell structure and the graded anisotropy, although both models give rise to similar overall results, the latter model gives a somewhat smoother approach to saturation, similar to what is observed experimentally. Thus, the simulations might hint at a possible graded anisotropy character to the nanoparticles.

4. Conclusions

Core/shell nanoparticles with a narrow size distribution have been synthesized using a seeded growth procedure. Two CS nanoparticles with different core size and equal shell thickness have been presented. Interestingly, in both cases an iron and manganese ion interdiffusion has been found, leading to an inverse soft/hard ferrimagnetic $Mn_xFe_{3-x}O_4/Fe_xMn_{3-x}O_4$ core/shell structure, as opposed to the conventional hard/soft systems. The particles display a strong exchange coupling between the soft core and hard shell as expected from the core and shell dimensions. The coupling also results in a loop shift along the field axis and a coercivity increase, which are more pronounced for the samples with smaller core size. Thus, the fine control of the

magnetic properties by the soft/hard coupling could render novel types of core/shell nanoparticles suitable for applications such as permanent magnets or in magnetic shielding.

References

1 W. Schärtl, *Nanoscale*, 2010, **2**, 829.
2 H. Zeng and S. Sun, *Adv. Funct. Mater.*, 2008, **18**, 391.
3 R. Costi, A. E. Saunders and U. Banin, *Angew. Chem., Int. Ed.*, 2010, **49**, 4878.
4 L. Carbone and P. D. Cozzoli, *Nano Today*, 2010, **5**, 449.
5 V. Skumryev, S. Stoyanov, Y. Zhang, G. Hadjipanayis, D. Givord and J. Nogués, *Nature*, 2003, **423**, 850.
6 J. Nogués, J. Sort, V. Langlais, V. Skumryev, S. Suriñach, J. S. Muñoz and M. D. Baró, *Phys. Rep.*, 2005, **422**, 65.
7 O. Iglesias, A. Labarta and X. Batlle, *J. Nanosci. Nanotechnol.*, 2008, **8**, 2761.
8 W. Liu, W. Zhong and Y. W. Du, *J. Nanosci. Nanotechnol.*, 2008, **8**, 2781.
9 I. S. Lee, N. Lee, J. Park, B. H. Kim, Y. W. Yi, T. K. Kim, I. H. Lee, S. R. Paik and T. Hyeon, *J. Am. Chem. Soc.*, 2006, **128**, 10658.
10 O. Masala and R. Seshadri, *J. Am. Chem. Soc.*, 2005, **127**, 9354.
11 D. W. Kavich, J. H. Dickerson, S. V. Mahajan, S. A. Hasan and J.-H. Park, *Phys. Rev. B: Condens. Matter Mater. Phys.*, 2008, **78**, 174414.
12 G. Salazar-Alvarez, J. Sort, S. Suriñach, M. D. Baró and J. Nogués, *J. Am. Chem. Soc.*, 2007, **129**, 9102.
13 I. V. Golosovsky, G. Salazar-Alvarez, A. López-Ortega, M. González, J. Sort, M. Estrader, S. Suriñach, M. D. Baró and J. Nogués, *Phys. Rev. Lett.*, 2009, **102**, 247201.
14 A. López-Ortega, D. Tobia, E. Winkler, I. V. Golosovsky, G. Salazar-Alvarez, S. Estradé, M. Estrader, J. Sort, M. A. González, S. Suriñach, J. Arbiol, F. Peiró, R. D. Zysler, M. D. Baró and J. Nogués, *J. Am. Chem. Soc.*, 2010, **132**, 9398.
15 E. E. Fullerton, J. S. Jiang and S. D. Bader, *J. Magn. Magn. Mater.*, 1999, **200**, 392.
16 R. H. Victora and X. Shen, *IEEE Trans. Magn.*, 2005, **41**, 537.
17 N. A. Frey, S. Peng, K. Cheng and S. Sun, *Chem. Soc. Rev.*, 2009, **38**, 2532.
18 H. Zeng, J. Li, J. P. Liu, Z. L. Wang and S. Sun, *Nature*, 2002, **420**, 395.
19 C. W. Kim, Y. H. Kim, H. G. Cha and Y. S. Kang, *Mol. Cryst. Liq. Cryst.*, 2007, **464**, 583.
20 C. W. Kim, Y. H. Kim, H. G. Cha, J. C. Kim and Y. S. Kang, *Mol. Cryst. Liq. Cryst.*, 2007, **472**, 545.
21 C. W. Kim, Y. H. Kim, D. K. Lee, I. C. Jeong, H. W. Kwon and Y. S. Kang, *Solid State Phenom.*, 2007, **119**, 147.
22 D. K. Lee, H. G. Cha, Y. H. Kim, C. W. Kim, E. S. Ji and Y. S. Kang, *J. Nanosci. Nanotechnol.*, 2009, **9**, 4453.
23 A. Figuerola, A. Fiore, R. D. Corato, A. Falqui, C. Giannini, E. Micotti, A. Lascialfari, M. Corti, R. Cingolani, T. Pellegrino, P. D. Cozzoli and L. Manna, *J. Am. Chem. Soc.*, 2008, **130**, 1477.

24 V. Nandwana, G. S. Chaubey, K. Yano, C.-B. Rong and J. P. Liu, *J. Appl. Phys.*, 2009, **105**, 014303.

25 G. S. Chaubey, V. Nandwana, N. Poudyal, C.-B. Rong and J. P. Liu, *Chem. Mater.*, 2008, **20**, 475.

26 H. Zeng, J. Li, Z. L. Wang, J. P. Liu and S. Sun, *Nano Lett.*, 2004, **4**, 187.

27 J. Kim, C. Rong, Y. Lee, J. P. Liu and S. Sun, *Chem. Mater.*, 2008, **20**, 7242.

28 L. C. Varanda, M. Imaizumi, F. J. Santos and M. Jafelicci, Jr, *IEEE Trans. Magn.*, 2008, **44**, 4448.

29 C. Liu, X. Wu, T. Klemmer, N. Shukla and D. Weller, *Chem. Mater.*, 2005, **17**, 620.

30 H. Zeng, S. Sun, J. Li, Z. L. Wang and J. P. Liu, *Appl. Phys. Lett.*, 2004, **85**, 792.

31 Q. K. Ong and A. Wei, *Phys. Rev. B: Condens. Matter Mater. Phys.*, 2009, **80**, 134418.

32 C. Wang, D. R. Baer, J. E. Amonette, M. H. Engelhard, J. Antony and Y. Qiang, *J. Am. Chem. Soc.*, 2009, **131**, 8824.

33 (a) O. Masala, D. Hoffman, N. Sundaran, K. Page, T. Proffen, G. Lawes and R. Seshadri, *Solid State Sci.*, 2006, **8**, 1015; (b) J.-H. Lee, J.-T. Jang, J.-S. Choi, S.-H. Moon, S.-H. Noh, J.-W. Kim, J.-G. Kim, I.-S. Kim, K.-I. Park and J. Cheon, *Nat. Nanotechnol.*, 2011, **6**, 418; (c) J. Cheon, J.-I. Park, J.-S. Choi, Y.-W. Jun, S. Kim, M. G. Kim, Y.-M. Kim and Y. J. Kim, *Proc. Natl. Acad. Sci. U. S. A.*, 2006, **103**, 3023.

34 J. H. Hong, W. S. Kim, J. I. Lee and N. H. Hur, *Solid State Commun.*, 2007, **141**, 541.

35 J. S. Jiang, J. E. Pearson, Z. Y. Liu, B. Kabius, S. Trasobares, D. J. Miller and S. D. Bader, *J. Appl. Phys.*, 2005, **97**, 10K311.

36 G. Salazar-Alvarez, J. Sort, A. Uheida, M. Muhammmed, S. Suriñach, M. D. Baró and J. Nogués, *J. Mater. Chem.*, 2007, **17**, 322.

37 A. J. Zambano, H. Oguchi, I. Takeuchi, Y. Choi, J. S. Jiang, J. P. Liu, S. E. Loftland, D. Josell and L. A. Bendersky, *Phys. Rev. B: Condens. Matter Mater. Phys.*, 2007, **75**, 144429.

38 (a) C. L. Zha, R. K. Dumas, Y. Y. Fang, V. Bonanni, J. Nogués and J. Åkerman, *Appl. Phys. Lett.*, 2010, **97**, 182504; (b) V. Bonanni, Y. Y. Fang, R. K. Dumas, C. L. Zha, S. Bonetti, J. Nogués and J. Åkerman, *Appl. Phys. Lett.*, 2010, **97**, 202501.

39 G. Salazar-Alvarez, H. Lidbaum, A. López-Ortega, M. Estrader, K. Leifer, J. Sort, S. Suriñach, M. D. Baró and J. Nogués, *J. Am. Chem. Soc.*, 2011, **133**, 16738.

40 J. Park, K. An, Y. Hwang, J. G. Park, H. J. Noh, J. Y. Kim, J. H. Park, N. M. Hwang and T. Hyeon, *Nat. Mater.*, 2004, **3**, 891.

41 (a) H. M. Rietveld, *Acta Crystallogr.*, 1966, **20**, 508; (b) J. Rodriguez-Carvajal, *Phys. B*, 1993, **192**, 55.

42 (a) K. R. Beyerlein, J. Solla-Gullón, E. Herrero, E. Garnier, F. Pailloux, M. Leoni, P. Scardi, R. L. Snyder, A. Aldaz and J. M. Feliu, *Mater. Sci. Eng., A*, 2010, **528**, 83; (b) I. V. Golosovsky, I. Mirebeau, E. Elkaim, D. A. Kurdyukov and Y. A. Kumzerov, *Eur. Phys. J. B*, 2005, **47**, 55.

43 C. R. Pike, A. P. Roberts and K. L. Verosub, *J. Appl. Phys.*, 1999, **85**, 6660.

44 (a) S.-J. Cho, A. M. Shahin, G. L. Long, J. E. Davies, K. Liu, F. Grandjean and S. M. Kauzlarich, *Chem. Mater.*, 2006, **18**, 960; (b) M. T. Rahman, R. K. Dumas, N. Eibagi, N. N. Shams, Y.-C. Wu, K. Liu and C. H. Lai, *Appl. Phys. Lett.*, 2009, **94**, 042507; (c) N. Sakuma, T. Ohshima, T. Shoji, Y. Suzuki, R. Sato, A. Wachi, A. Kato, Y. Kawai, A. Manabe and T. Teranishi, *ACS Nano*, 2011, **5**, 2806.

45 J. E. Davies, O. Hellwig, E. E. Fullerton, J. S. Jiang, S. D. Bader, G. T. Zimanyi and K. Liu, *Appl. Phys. Lett.*, 2005, **86**, 262503.

46 R. K. Dumas, C. L. Zha, Y. Y. Fang, V. Bonanni, J. W. Lau, J. Nogués and J. Åkerman, *IEEE Trans. Magn.*, 2011, **47**, 1580.

47 D. Suess, *Appl. Phys. Lett.*, 2006, **89**, 113105.

48 K. Binder, in *Applications of Monte Carlo Methods in Statistical Physics*, Springer, Berlin, 1984.

49 V. Baron, J. Gutzmer, H. Rundlöf and R. Tellegren, *Am. Mineral.*, 1998, **83**, 786.

50 (a) P. Franke and R. Dieckman, *Solid State Ionics*, 1989, **817**, 32; (b) H. Meher, in *Diffusion in Solids, Fundamentals, Methods, Materials, Diffusion-Controlled Processes*, Springer-Verlag, Berlin, 2007.

51 M. Abbate, J. B. Goedkoop, F. De Groot, M. Grioni, J. C. Fuggle, S. Hofmann, H. Petersen and M. Sacchi, *Surf. Interface Anal.*, 1992, **18**, 65.

52 H. J. Lee, G. Kim, D. H. Kim, J.-S. Kang, C. L. Zhang, S. W. Cheong, J. H. Shim, S. Lee, H. Lee, J.-Y. Kim, B. H. Kim and B. I. Min, *J. Phys.: Condens. Matter*, 2008, **20**, 295203.

53 E. Pellegrin, M. Hagelstein, S. Doyle, H. O. Moser, J. Fuchs, D. Vollath, S. Schuppler, M. A. James, S. S. Saxena, L. Niesen, O. Rogojanu, G. A. Sawatzky, C. Ferrero, M. Borowski, O. Tjernberg and N. B. Brookes, *Phys. Status Solidi B*, 1999, **215**, 797.

54 C. L. Chen, Electronic and Magnetic Properties of Transition Metal Ferrites and Superlattice Studied by X-ray Absorption Spectroscopy, PhD thesis, Tamkang University, Tamsui, Taiwan, 2005.

55 V. Bayer, R. Podloucky, C. Franchini, F. Allegretti, B. Xu, G. Parteder, M. G. Ramsey, S. Surnev and F. P. Netzer, *Phys. Rev. B: Condens. Matter Mater. Phys.*, 2007, **76**, 165428.

56 V. Pool, M. Klem, C. Jolley, E. A. Arenholz, T. Douglas, M. Young and Y. U. Idzerda, *J. Appl. Phys.*, 2010, **107**, 09B517.

57 M. Knobel, W. C. L. Nunes, M. Socolovsky, E. De Biasi, J. M. Vargas and J. C. Denardin, *J. Nanosci. Nanotechnol.*, 2008, **8**, 2836.

58 W. Palmer, *J. Appl. Phys.*, 1962, **33**, 1201.

59 B. Boucher, R. Buhl and M. Perrin, *J. Appl. Phys.*, 1969, **40**, 1126.

60 R. Gerber, Z. Šimša and M. Vicher, *Czech. J. Phys.*, 1963, **16**, 913.

61 T. Battault, R. Legros and A. Rousset, *J. Eur. Ceram. Soc.*, 1995, **15**, 1141.

62 A. H. Eschenfelder, *J. Appl. Phys.*, 1958, **29**, 378.

63 K. Dwight and N. Menyuk, *Phys. Rev.*, 1960, **119**, 1470.

64 J. Kub, V. Brabers, P. Novák, R. Gemperle and J. Šimšová, *J. Magn. Magn. Mater.*, 2000, **217**, 19.

65 K. Abe, Y. Miyamoto and S. Chikazumi, *J. Phys. Soc. Jpn.*, 1976, **41**, 1894.